https://doi.org/10.1016/j.enconman.2021.113827

Enabling thermal-neutral electrolysis for CO_2-to-fuel conversions with a hybrid deep learning strategy

Haoran Xu[1#], Jingbo Ma[2#], Peng Tan[3], Zhen Wu[4], Yanxiang Zhang[2], Meng Ni[5,6*], Jin Xuan[1*]

[1] Department of Chemical Engineering, Loughborough University, Loughborough, United Kingdom

[2] National Key Laboratory for Precision Hot Processing of Metals, School of Materials Science and Engineering, Harbin Institute of Technology, Harbin, Heilongjiang, 150001, China

[3] Department of Thermal Science and Energy Engineering, University of Science and Technology of China, Hefei, 230026, China

[4] Shaanxi Key Laboratory of Energy Chemical Process Intensification, School of Chemical Engineering and Technology, Xi'an Jiaotong University, Xi'an, China

[5] Building Energy Research Group, Department of Building and Real Estate

The Hong Kong Polytechnic University, Hung Hom, Kowloon, Hong Kong, China

[6] Environmental Energy Research Group, Research Institute for Sustainable Urban Development (RISUD), The Hong Kong Polytechnic University, Hung Hom, Kowloon, Hong Kong, China

Abstract

High-temperature co-electrolysis of CO_2/H_2O through the solid oxide electrolysis cells (SOECs) is a promising method to generate renewable fuels and chemical feedstocks. Applying this technology in flexible scenario, especially when combined with variable renewable powers, requires an efficient optimisation strategy to ensure its safety and cost-effective in the long-term operation. To this purpose, we present a hybrid simulation method for the accurate and fast optimisation of the co-electrolysis process in the SOECs. This method builds multi-physics models based on experimental data and extends the database to develop the deep neural network and genetic algorithm. In the case study, thermal-neutral condition (TNC) is set as the optimisation target in various operating conditions, where the SOEC generates no waste heat and needs no auxiliary heating equipment. Small peak-temperature-gradient (PTG) inside the SOEC is found at the TNC, which is vital to prevent thermal failure in the operation. For the cell operating with 1023 K and 1123 K of inlet gas temperatures, the smallest PTGs reach 0.09 and 0.31 K mm^{-1} at 1.13 and 1.19 V, respectively. Finally, a 4-D map is presented to show the interactions among the applied voltage, required power density, inlet gas composition, and temperature under the TNC. The proposed method can be flexibly modified based on different optimisation targets for various applications in the energy sector.

Keywords: Solid oxide electrolyser; Co-electrolysis; Renewable energy; Artificial intelligence; Genetic algorithm; Hybrid simulation.

# These authors contributed equally to this paper

* Corresponding authors:

Email: J.Xuan@lboro.ac.uk; Tel: +44 (0)1509 227186 (Jin Xuan)

Email: meng.ni@polyu.edu.hk; Tel: 852-27664152; Fax: 852-27645131 (Meng NI).

1. Introduction

For the long-term prosperity of human society, the idea of sustainable development is becoming a worldwide consensus [1]. The global climate change caused by the growing CO_2 level in the atmosphere is one of the largest threats [2]. To reduce the CO_2 level, the value-added utilisation of CO_2 is a key step, where positive feedback from the market will boost the development of CO_2 capture and storage technologies [3]. Solid oxide electrolysis cell (SOECs) is an advanced technology in reducing oxidants to generate fuels by consuming electricity power [4,5]. When renewable powers are supplied to the SOEC, green fuels can be generated by electrolysing CO_2 and/or H_2O in the SOECs [6,7]. These green fuels can be further utilised through the Fischer-Tropsch process to generate the valuable hydrocarbons [8,9]. The reversible nature and the easily scalable characteristics of the SOEC allow it to work in the hybrid systems [10,11], making the SOEC promising for a wide range of application.

SOECs usually work at high temperatures (> 700 ^{o}C), which brings high reaction activity and enables the use of non-noble catalysts (such as nickel). The catalyst flexibility allows the appearance of many gas components (e.g. CO), which could be toxic to the low-temperature electrolysers [12]. However, the sensitivity to temperature brings challenges in the heat management of SOECs [13]. With the change of operating parameters, SOECs may adsorb heat (e.g. at small applied voltages) or generate heat (e.g. at large applied voltages). To maintain the operation of SOECs and avoid the generation of waste heat, the auxiliary heating equipment is usually needed [14]. Thermal-neutral condition (TNC) is a special status of SOECs, where the heat needed for endothermic processes is equal to the heat generated in exothermic processes [15]. In this situation, the SOECs can maintain its operation without external heat supply and waste heat generation.

Operating conditions including the applied voltage, inlet gas flow rate, operating temperature and inner pressure have shown great effects to the performance of the SOEC [16,17]. To keep the SOEC working at the TNC under different operating parameters, a fast and accurate online optimisation method is required. Currently, the widely used methods only fits part of the requirements for efficient optimisation of SOECs. One method is the widely developed numerical models using multi-physics simulation (MPS)[18,19]. The MPS considers the detailed effects of mass/momentum transport, electrochemical/chemical reactions, and heat transfer. It can accurately predict the performance of SOECs under various operating conditions. However, MPS usually costs many computing resources to find the optimised results, making it unsuitable for online optimisation purpose.

On the other hand, the data-driven models (such as deep neural network, DNN) can cost-effectively predict the results under the given input parameters [20,21]. When combined with the genetic algorithm (GA), fast online optimisation can be further achieved [22]. In recent years, combing machine learning with energy science, theoretical physical chemistry and material science becomes popular as machine learning offers a new sight into traditional scientific phenomenon [23]. Deep learning treats a system with constant input and output to be black box and uses its own way to understand the map from input to output [24]. With this unique feature, deep learning is a useful and powerful tool in analysing the electrochemical system [25]. However, the accuracy of data-driven models is largely limited by the generation of high quality training dataset, making them too expensive for most application scenarios.

To date, there is still lack of a reliable predictive toolbox for real time prediction and optimisation of complex multi-physics processes such as SOEC for CO_2-to-fuel conversions. The optimisation of SOEC with the limitation conditions regarding the unmeasurable parameters (such as the heat generation in operation) is especially difficult. Herein, we propose a hybrid method that combines experimental data, MPS, DNN, and GA to overcome the complexity and substantive costing in the fast and accurate optimisation of SOECs. For the first time, we demonstrate a DNN-informed status tracking method that allows SOEC to maintain thermal balance subject to changes in its operation conditions. And the fast optimisation with the limitation of any numerically calculable parameter of the SOEC is proved to be achievable.

2. Model Development

2.1 Schematic and framework

Fig. 1 shows a schematic of an SOEC for H_2O and CO_2 co-electrolysis. In the SOEC, oxidants are reduced into fuels and O^{2-} by accepting electrons from external power sources. O^{2-} ions transport through the dense electrolyte to the cathode, where O_2 is generated and electrons are released through the external circuit.

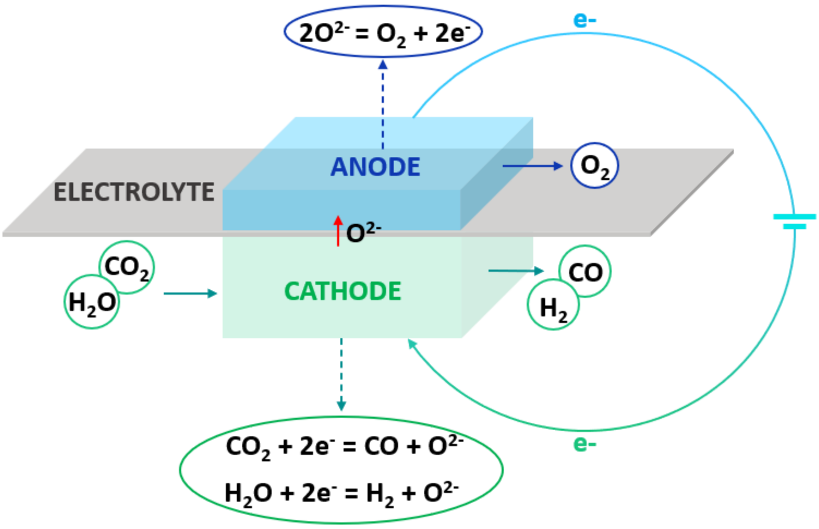

Fig. 1 The schematic of an SOEC for H_2O and CO_2 co-electrolysis.

The workflow of the hybrid method is presented in Fig. 2. First, the multi-physics model of the SOEC is developed and validated in accordance with the experimental results. A database is then generated with sets of parameters (including the temperature, gas flow rate, gas composition at inlets and outlets, voltage, current density, and heat). The extended database is used to train the DNN algorithm, where the relationship among input/output parameters is mapped. Finally, the well-trained DNN algorithm is adopted as the fitness function in GA to predict the optimised parameters of SOECs.

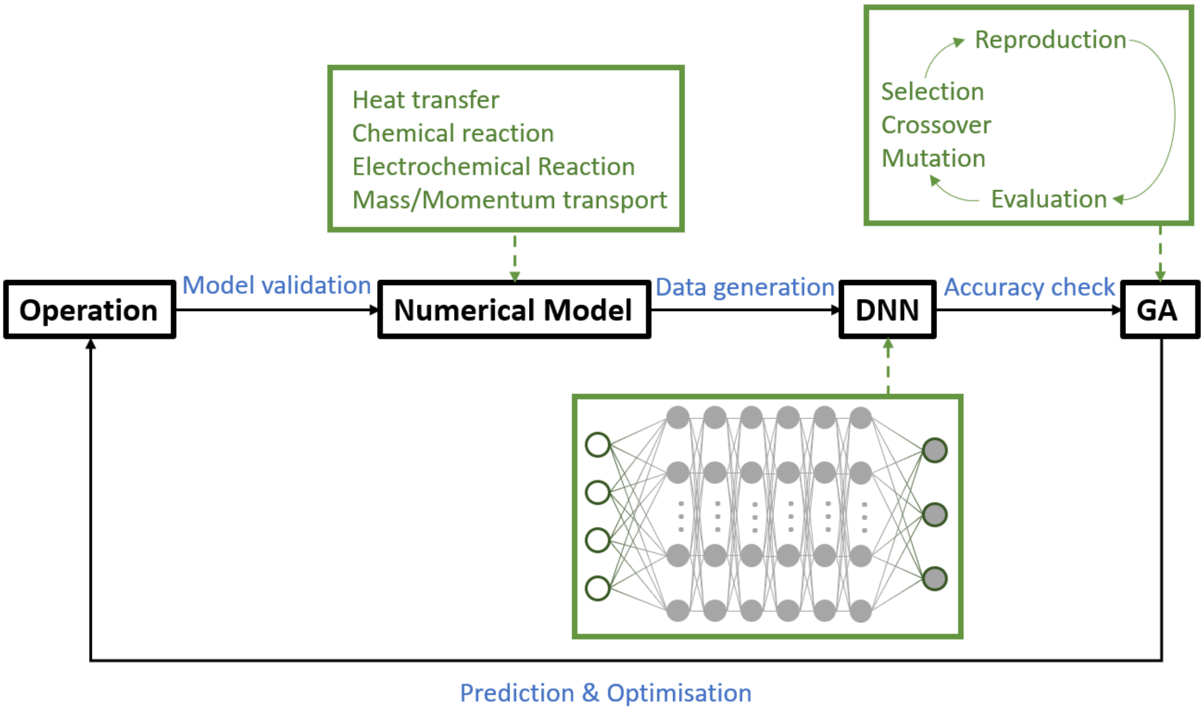

Fig. 2 The workflow of the hybrid method for the optimisation of SOECs.

2.2 Model assumptions and boundary conditions for the MPS model

For model simplification and easier calculation, below assumptions are adopted in the MPS model:

(1) The electrochemical reactions occur at triple-phase boundaries, which distribute uniformly in the porous anode and cathode as the materials are well mixed in the electrode preparing.

(2) Ion/electron conducting phases and porous medium are continuous and evenly distributed as the ionic and electronic conducting materials are well mixed in the electrode preparing.

(3) The gas at the cathode inlet contains only H_2O and CO_2, and all the gas species are ideal because the effects of intermolecular forces and molecules sizes are less significant at high operating temperature.

(4) Heat loss caused by thermal radiation is neglected as the SOEC is considered to be an adiabatic system.

Apart from these assumptions, below boundary conditions are also applied in the MPS model:

(1) The values of voltage are specified at the outside surface of the anode and cathode.

(2) The values of flow rate, composition, and temperature of the gas are specified at the chamber inlets of anode and cathode.

(3) Free flow condition is specified at the chamber outlets at the anode and cathode.

(4) Zero flux and thermal insulation are specified at the ends of electrodes and the outside surface of the cell.

2.3 Development of the MPS model for SOEC

The experimental data of a SOEC presented by Li et al.[26] is adopted for the development and validation of the MPS model. In their work, the co-electrolysis of CO2 and H2O is successfully conducted using the cell with commercially available materials, Ni-YSZ, Ni-ScSZ and LSM-ScSZ as the cathode (680 um in thickness), electrolyte (15 um in thickness) and anode (20 um in thickness), respectively. They also studied the cell performance at various operating conditions, making the work suitable for model development and validation. To study the temperature distribution effects, the cell structure is extended to a tubular cell with a length of

70 mm in the subsequent parametric studies. Processes including heat transfer, chemical reaction, electrochemical reaction, and mass/momentum transport are combined to describe the complex phenomena in the SOEC. The governing equations are listed in Table 1, for which the detailed description can be found in our previous works [27,28]. The model is solved in a commercial nonlinear finite element solver, COMSOL Multiphysics.

2.3.1 Electrochemistry

In the fuel electrode (cathode), the mixture of H_2O and CO_2 is introduced. Driven by applied voltages, H_2O and CO_2 are reduced as given from Eqs. (1)-(2).

$$\mathrm{H_2O + 2e^- = H_2 + O^{2-}} \tag{1}$$

$$\mathrm{CO_2 + 2e^- = CO + O^{2-}} \tag{2}$$

In the air electrode (anode), the O^{2-} ions release electrons and form O_2 as given in Eq. (3).

$$\mathrm{O^{2-} = 0.5O_2 + 2e^-} \tag{3}$$

Along with the internal travel of O^{2-} from cathode to anode, the electrons travel from anode to cathode through external circuit. To close the cycle, a certain voltage (V) is applied as shown in Eq. (4).

$$\mathrm{V = E_{eq} + \eta_{act} + \eta_{ohmic}} \tag{4}$$

Here, $\mathrm{E_{eq}}$, $\mathrm{\eta_{act}}$ and $\mathrm{\eta_{ohmic}}$ are the equilibrium voltage, activation overpotential and ohmic overpotential. To reduce H_2O and CO_2, the equilibrium potentials ($\mathrm{E_{eq,H_2O}}$ and $\mathrm{E_{eq,CO_2}}$) are calculated by Nernst Equation as given in Eqs. (5)-(6), respectively.

$$\mathrm{E_{eq,H_2O} = E^0_{eq,H_2O} + \frac{RT}{2F} ln\left[\frac{P^{L,C}_{H_2}(P^{L,A}_{O_2})^{1/2}}{P^{L,C}_{H_2O}}\right]} \tag{5}$$

$$\mathrm{E_{eq,CO_2} = E^0_{eq,CO_2} + \frac{RT}{2F} ln\left[\frac{P^{L,C}_{CO}(P^{L,A}_{O_2})^{1/2}}{P^{L,C}_{CO_2}}\right]} \tag{6}$$

Here E^0_{eq,H_2O} and E^0_{eq,CO_2} are standard values of equilibrium potentials for the electrolysis of H_2O and CO_2, respectively. $P^{L,C}$ and $P^{L,A}$ are local partial pressures at the cathode and the anode, respectively. As the local partial pressure is adopted for calculation, the so-called concentration overpotential will not be considered.

η_{act} reflects the energy barrier in the electrochemical reaction, which is calculated using the Butler-Volmer equation as shown in Eq. (7).

$$i = i_0 \left\{ \exp\left(\frac{\alpha n F \eta_{act}}{RT}\right) - \exp\left(-\frac{(1-\alpha) n F \eta_{act}}{RT}\right) \right\} \quad (7)$$

The value of exchange current density (i_0) for H_2O electrolysis is set to be 2.2 times of the i_0 for CO_2 electrolysis as suggested by the experiments [26].

η_{ohmic} is calculated using Ohm’s law. The ionic resistance and electronic resistance are calculated separately as given in Eqs. (8)-(9).

$$i_l = -{\sigma_l}^{eff} \nabla(\emptyset_l) \quad (8)$$

$$i_s = -{\sigma_s}^{eff} \nabla(\emptyset_s) \quad (9)$$

2.3.2 Chemical reaction

Due to the existence of H_2O, CO_2, H_2 and CO, the water gas shift reaction (WGSR) is very important in balancing the concentration of the inner gas compositions. Due to the huge difference in reaction rates with and without catalysts, the WGSR is considered on the area with nickel catalyst as given in Eq. (10).

$$CO + H_2O \leftrightarrow CO_2 + H_2 \quad (10)$$

2.3.3 Fluid flow

The transport properties of the gases are adopted according to Young’s work [29]. Free molecule diffusion and Knudsen diffusion are considered for the mass transport in gas channels and porous areas by using the dusty-gas model as shown in Eq. (11).

$$\frac{\mathrm{N_i}}{\mathrm{D_{ik}^{eff}}} + \sum_{j=1, j\neq i}^{n} \frac{\mathrm{y_j N_i - y_i N_j}}{\mathrm{D_{ij}^{eff}}} = -\frac{1}{\mathrm{RT}}\left(\nabla\left(\mathrm{y_j P}\right) + \frac{\mathrm{B_0 y_j P}}{\mathrm{\mu D_{ik}^{eff}}}\nabla \mathrm{P}\right) \tag{11}$$

The mass conservation in steady states is calculated using Eq. (12).

$$\nabla \cdot \mathrm{N_j} = \mathrm{S_j} \tag{12}$$

Momentum transport is calculated using Navier–Stokes (N-S) equation as shown in Eq. (13).

$$\rho\frac{\partial \mathrm{u}}{\partial \mathrm{t}} + \rho \mathrm{u}\nabla \mathrm{u} = -\nabla \mathrm{p} + \nabla[\mu\left(\nabla \mathrm{u} + (\nabla \mathrm{u})^{\mathrm{T}}\right) - \frac{2}{3}\mu\nabla \mathrm{u}\Big] - \frac{\varepsilon\mu \mathrm{u}}{\mathrm{k}} \tag{13}$$

2.3.4 Heat transfer

Heat transfer process in steady state is calculated by heat balance equation as shown in Eq. (14).

$$\rho \mathrm{C_p} \mathrm{u} \cdot \nabla \mathrm{T} + \nabla \cdot (-\lambda_{\mathrm{eff}} \nabla \mathrm{T}) = \mathrm{Q} \tag{14}$$

2.4 Development of deep learning (DL) algorithms

2.4.1 Deep neural network

DNN can capture the functional relationship between input-output pairs without presumptions [30]. Its computational topology consists of an input layer, multiple hidden layers, and an output layer. The layers have processing units, which receive multiple inputs with connection weights. In each layer, the inputs are transformed with an activation function (ReLU or linear) to generate the outputs. These outputs are then processed as inputs in the next layer [31].

In this study, a back-propagation DNN (BP-DNN) is adopted with a structure of one input payer (four nodes), six hidden layers, and one output layer (three nodes). The input parameters are the applied voltage, the gas composition at the cathode inlet, the gas flow rate at the cathode inlet, and the temperature at the inlets. The outputs are the generated heat, current density, and gas composition at the cathode outlet. A 7211 × 7 dataset is split into a training set (80%) and a testing set (20%). 2000 epochs are set with a batch size of 32.

2.4.1.1 Pre-process of dataset

Parameters normalization is firstly conducted because the inlet parameters have different orders of magnitude, ranging from 10^{-1} to 10^{3}. The normalization process is accomplished by scaling all data within a uniform range as shown in Eq. (15) [32].

$$x_i = 0.8\left(\frac{k_i - k_{min}}{k_{max} - k_{min}}\right) + 0.1 \tag{15}$$

Here x_i, k_i, k_{min}, k_{max} are the normalized, actual, the minimum and the maximum values of the data, respectively.

2.4.1.2 Determination of network structure

The least mean square error (MSE) and correlation coefficient (r) are chosen as the criteria to evaluate the performance of the DNN algorithm as shown in Eq. (16) and (17).

$$\mathrm{MSE} = \frac{1}{\mathrm{M}}\sum_{\mathrm{i}=1}^{\mathrm{M}}(\mathrm{x_i} - \widehat{\mathrm{x_i}})^2 \tag{16}$$

$$\mathrm{r} = \mathrm{Correl}(\mathrm{x_i}, \widehat{\mathrm{x_i}}) = \frac{\mathrm{Cov}(\mathrm{x_i}, \widehat{\mathrm{x_i}})}{\sigma_{\mathrm{x_i}}\sigma_{\widehat{\mathrm{x_i}}}} \tag{17}$$

Here M is the number of data, $\widehat{\mathrm{x_i}}$ is the value of the data predicted by the DNN algorithm. $\sigma_{\mathrm{x_i}}$, $\sigma_{\widehat{\mathrm{x_i}}}$, $\mathrm{Cov}(\mathrm{x_i}, \widehat{\mathrm{x_i}})$ are the variances and covariance of the two datasets generated by the MPS and DNN algorithms.

2.4.2 Genetic algorithm

GA is a popular evolutionary algorithm widely used in global optimisation problems. Starting from random strings (initial population), it generates offspring through three operators: selection, crossover, and mutation. Fitness function (the trained DNN algorithm) is adopted to evaluate the candidates, after which the qualified individuals are more likely to be chosen for reproduction. Such an iteration continues until the stop criteria are reached.

The population, generation, crossover rate, mutation frequency, and tournament size are set as 100, 100, 0.8, 0.2 and 5, respectively. The optimisation criterion is the minimum heat generation/adsorption ($< 10^{-7}$) as shown in Eq. (18).

$$|Q| < 10^{-7} \text{ (J)} \quad (18)$$

3. Results and Discussion

First, parametric studies are conducted using the validated MPS model. The key operating parameters such as the applied voltage, temperature, gas composition, and flow rate at the inlets are studied to investigate their effects on the SOEC performance, including the current/power density, fuel conversion rate, heat generation, and peak-temperature-gradient (PTG). The MPS results form a database to train a DNN algorithm, which is used in the GA for performance prediction and optimisation. In this work, the optimisation targets are the values of operating parameters at the TNC of the SOEC. The operating parameters of the below parametric studies are listed in Table 5 to 7.

3.1 Model validation

3.1.1 Validation of the multi-physics simulation

The MPS model is validated by comparing the simulation results with experimental data at the same operating conditions (given in Table 2 to 4). The two sets of data show high consistence at the low operating voltages, while there are some relative large differences at high operating voltages. Overall, a small difference (correlation efficient, r = 0.994) is observed as shown in Fig. 3.

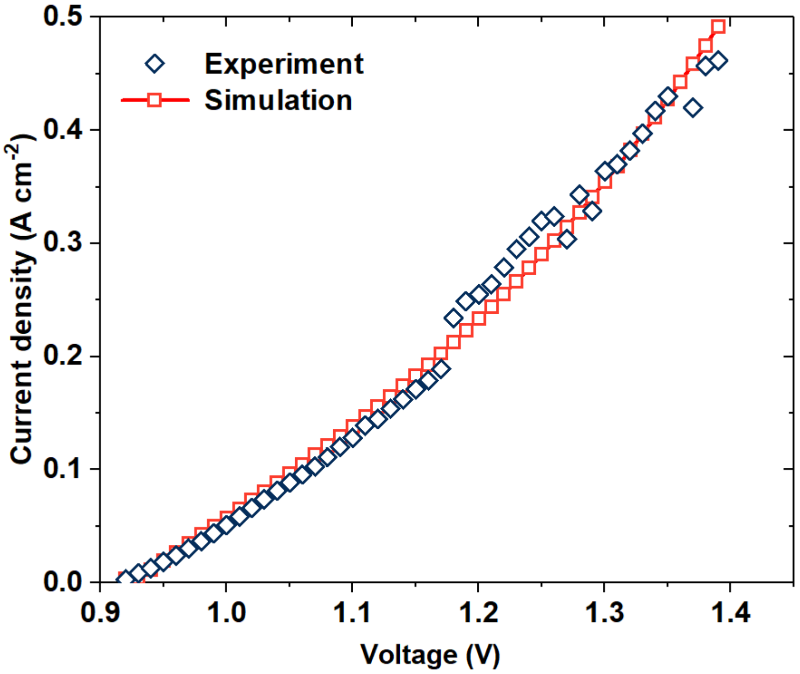

Fig. 3 Validation of the simulation results by comparing with the experimental data.

3.1.2 Validation of the deep neural network

10000 epochs are applied to train the DNN algorithm. While as shown in Fig. 4, it converges quickly after 10 epochs. The final correlation coefficient in the training set and testing set are 0.999976 and 0.999259, respectively. The final least mean square error in the training set and testing set are 0.0000024 and 0.000133, respectively.

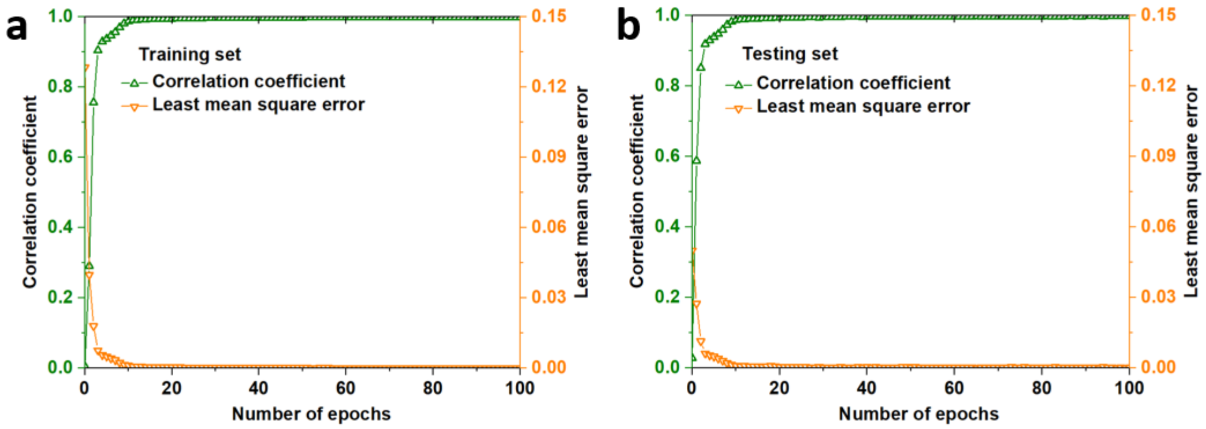

Fig. 4 The change of correlation coefficient and least mean square error in training and testing sets with the growth of epochs.

The distributions of the relative error in the prediction of current density, H_2 conversion rate and heat generation using DNN are presented in Fig. 5. Most of the predicted results show a small relative error, where 73% predicted current density, 50% predicted fuel generation rate and 54% predicted heat generation have relative errors less than 1%, 1%, and 3%, respectively.

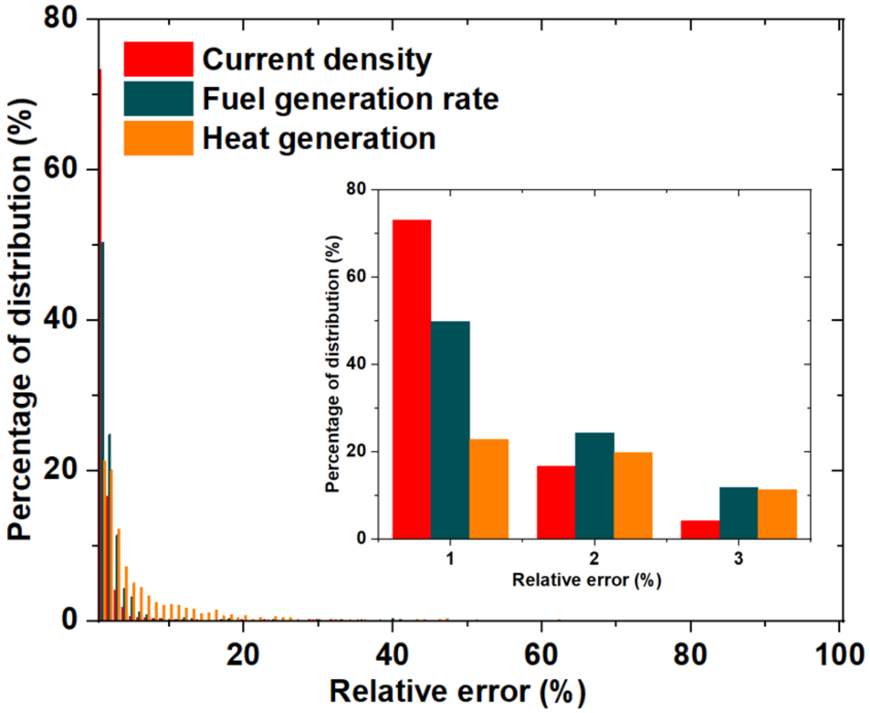

Fig. 5 The distribution of relative errors in predicting the current density, fuel generation rate and heat generation using DNN.

3.2 Effects of fluid flow rate and composition

Compared with a low flow rate (300 sccm), the high flow rate (600 sccm) allows a larger current density at high operating potentials, as shown in Fig 6a. In the 90% H_2O case, the limiting current density at 300 sccm is about 1.6 A cm^{-2} at 1.34 V, while the current density at 600 sccm reaches 2.3 A cm^{-2}. On the other hand, the low flow rate brings a much higher conversion rate, where the H_2 generation rate reaches 96% in 300 sccm case at 1.34 V. For comparison, the H_2 generation rate is 54% in 600 sccm case at 1.34 V as shown in Fig. 6b.

All the studied cases show a negative heat generation at low voltages, as shown in Fig. 6c, because the heat consumed in the endothermic processes (entropy change in electrochemical reactions) is larger than the heat generated in exothermic processes (activation overpotential and ohmic overpotential). Compared with the high flow rate and H_2O percentage case, a lower flow rate and H_2O percentage results in a more negative heat generation, between which the gas composition show a larger effect. With the increase of applied voltage, the heat generation reaches 0 in all the cases. This thermal-neutral point (TNP) is very important because neither the extra heat supply from auxiliary equipment will be needed to maintain the operation of SOECs nor the waste heat will be generated that reduces the efficiency of SOECs. In addition, the smallest PTG point is very close to the TNP, as shown in Fig. 6d. For the cell operating with 10% and 90% H_2O as the feedstock (CO_2 as the rest component), the smallest PTGs reach 0.21 and 0.17 K mm^{-1} at 1.41 and 1.11 V, respectively. As an even temperature distribution is crucial in reducing thermal stress and related thermal failure problems in the long-term operation of SOECs, the TNP brings additional benefits to the safe operation of SOECs.

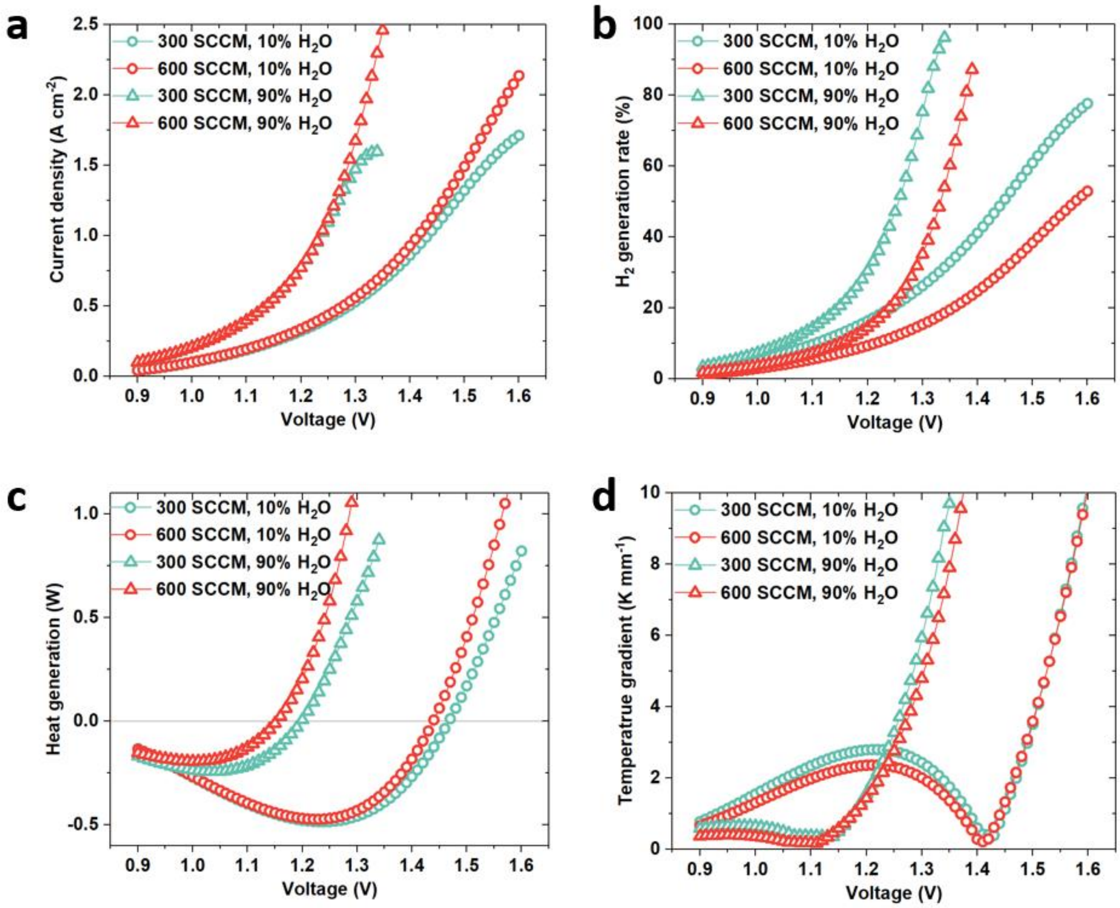

Fig. 6 Comparison of the SOEC performance at different applied voltages. The selected operating conditions are the combinations of flow rate (300/600 sccm) and gas composition (10%/90% H_2O) at the cathode inlet. (a) The voltage-current density relationship, (b) the voltage-H_2 generation rate relationship, (c) the voltage-heat generation relationship, and (d) the voltage-PTG relationship.

3.3 Effects of gas temperature at the inlet

Compared with the low temperature (1023K), the high temperature (1123K) at cathode inlet significantly improves the current density, as shown in Fig. 7a. The H_2 generation rate is highly correlated with the power density, indicates a smaller voltage is needed with the higher temperature at cathode inlet (Fig. 7b). Because of the improved electrochemical activity at the high operating temperature, more heat is consumed in endothermic processes at low voltages, which causes a more negative heat generation (Fig. 7c). With the increasing of the applied voltage, increased heat generation is observed at high temperatures due to the significantly raised current density and exothermic overpotential process. Although the high temperature case shows a larger PTG in most applied voltages, as shown in Fig. 7d, the significant decline of the PTG is observed near the TNP. At 1.19 V, the smallest PTG in the high temperature case is only 0.31 K mm^{-1}, even lower than that in the low temperature case (0.38 K mm^{-1}).

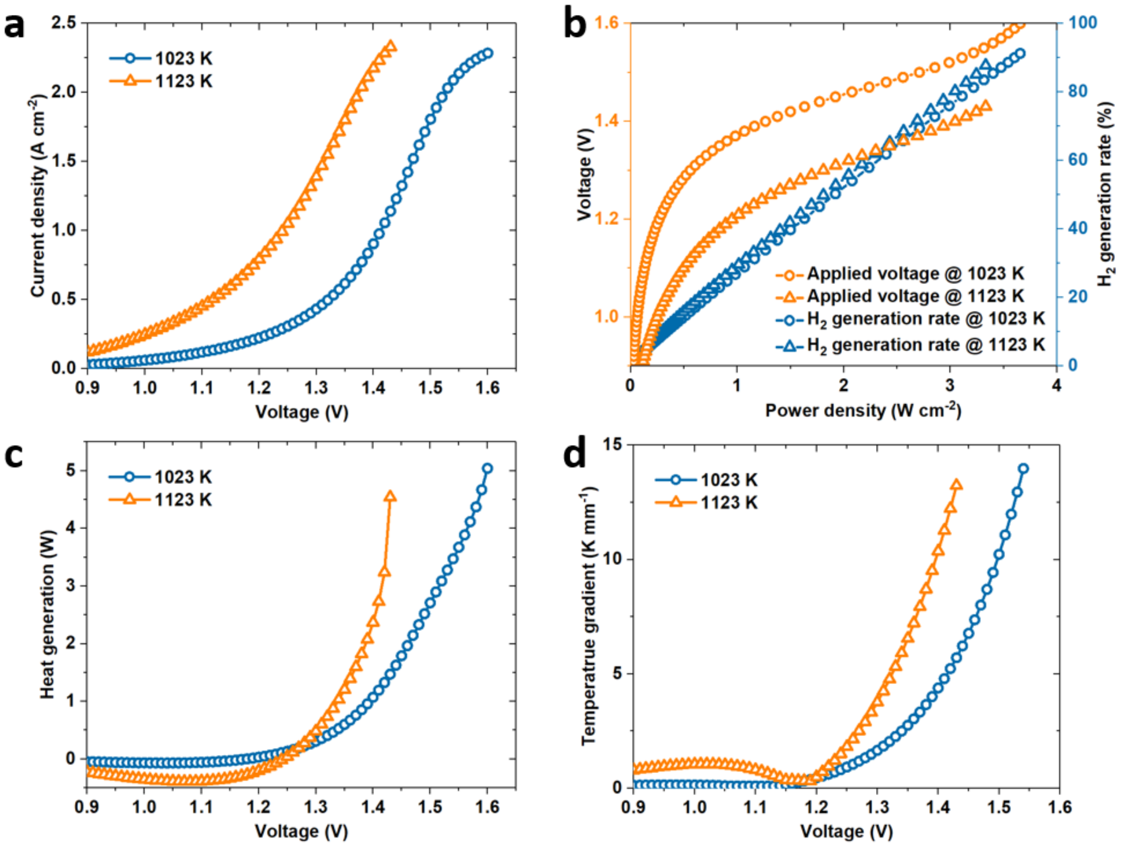

Fig. 7 Comparison of the SOEC performance at different inlet gas temperatures of 1023 and 1123 K under different applied voltages. (a) The voltage-current density relationship, (b) the power density-voltage-H_2 generation rate relationship, (c) the voltage-heat generation relationship, and (d) the voltage-PTG relationship.

3.4 Optimisation for thermal-neutral condition

As discussed above, working at the TNC simplifies system structure (no auxiliary heating equipment), improves system efficiency (no waste heat), and ensures a safe operating condition (small PTG) that avoids the thermal failure. The parameters of the TNC are thus the optimisation targets in the SOEC operation.

In this section, GA is adopted for performance prediction and optimisation based on the DNN. In GA, the optimisation target is the operating parameters including the fluid flow rate, composition, inlet temperature, voltage and current density at the TNC (i.e. $|Q| < 10^{-7}$ J). Meanwhile, the flow rate is set to between 300 and 600 sccm; the gas temperature at inlets is sect to between 1023 and 1123K; the mole fraction of H_2O at the cathode inlet is set between 0.1 and 0.9 (where the rest gas is CO_2). It needs to be pointed out that the GA with DNN algorithm incorporated significantly reduces the computational time. For GA, it takes about 0.6 second to predict an optimised point, whereas, for MPS method, it takes more than 60 seconds to do only the calculation, let alone the tremendous time required for searching for the optimised operating condition.

Fig. 8 shows the four-dimension map among power density, temperature, gas composition, and voltage in the TNC predicted by the GA. In the 3D Fig. 8(a), the x-axis, y-axis and z-axis are inlet H2O mole fraction, temperature, and power density, respectively. The 2D figures 8(b), 8(c) and 8(d) are the x-y projection, x-z projection and y-z projection of Fig. 8(a), respectively. For the co-electrolysis of H_2O and CO_2, working at the high H_2O mole fraction (low CO_2 level) and low operating temperature indicates a low applied voltage and required power density. For instance, when the cathode inlet gas contains 90% H_2O (10% CO_2 as rest gas) with a temperature of 1023K, the TNC requires only 1.124 V as applied voltage and 0.258 W cm^{-2} as input power density. On the other hand, the high CO_2 mole fraction (low H_2O level) and high working temperature means the high applied voltage and required power density, where these values at 90% CO_2 and 1123 K condition are 1.527 V and 2.801 W cm^{-2}, respectively. For comparison, the TNC at lowest-H2O-temperature case requires 1.38 V as applied voltage and 0.721 W cm^{-2} as input power density, while the TNC at highest-H2O-temperature case requires 1.23 V as applied voltage and 1.946 W cm^{-2} as input power density, both between the above two cases. Compared with the inlet H2O mole fraction, the operating temperature shows a much larger effect in decreasing the power density at TNC. There are selections among the fuel composition, production rate, and power consumption, where a high production rate and high CO percentage in the generated syngas usually requires a high voltage and power input. Therefore, a careful decision is still needed in the operation.

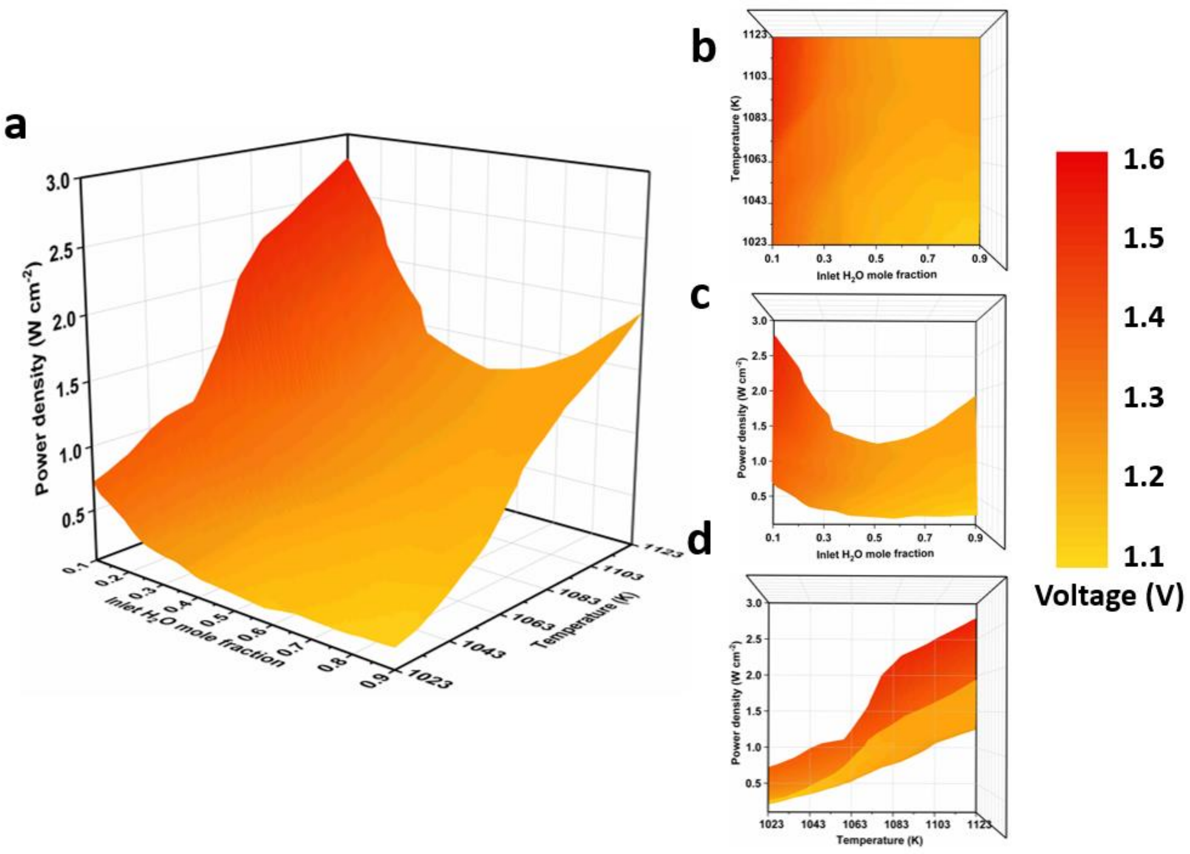

Fig. 8 (a) The distribution of required power density and applied voltage at different gas compositions and temperatures of cathode inlet under the TNC, (b) the voltage-temperature-gas composition relationship, (c) the voltage-power-gas composition relationship, and (d) the voltage-power-temperature relationship.

4. Conclusion

To predict the optimised working parameters of SOECs at the thermal-neutral condition (TNC), a hybrid method is developed combing experiments, multi-physics simulation and deep learning algorithms.

First, the multi-physics model is developed and validated based on the experimental data. The model is used to analyse the effects of different operating parameters on the performance of SOECs and generate an extended database for the training of the deep neural network. The thermal-neutral points are found to be significantly affected by the applied voltage (0.9~1.6 V), gas composition (H_2O, CO_2), and operating temperature (1023K vs. 1123K) at the SOEC inlet. The preliminary analysis shows a close relationship between the TNC and lowest peak-temperature-gradient in the cell, indicating its importance to the long-term operation of SOECs.

A 7211 × 7 database is generated using the validated multi-physics model for the training of the deep neural network. An effective neural network with a high correlation coefficient (> 0.999) is obtained and applied in the subsequent genetic algorithm. Finally, a four-dimensional map among the gas composition (10~90%), temperature (1023~1123K), voltage (0.9~1.6 V), and power density (0~3 W cm^{-2}) is successfully obtained under the TNC of the SOEC. As indicated by the map, the high CO_2 percentage and high working temperature require a high applied voltage as well as a high power to achieve the TNC.

The proposed method provides an alternative strategy for fast and accurate prediction and optimisation of SOECs. This method shows great potential and can be applied to other complex systems for a wide range of optimisation targets for energy decarbonisation applications. Although the working conditions in this preliminary work is relatively narrow, the operating parameters can be further expanded to a wider range in the future work and practical applications.

Data Availability

The data produced by MPS for the training and testing of DNN algorithm is available at https://github.com/Ma-Jingbo/SOEC-AI-Haoran-Xu.

Code Availability

The Keras package is available from [33]. The code for the DNN and GA are available at https://github.com/Ma-Jingbo/SOEC-AI-Haoran-Xu.

Acknowledgment

M. Ni would like to thank the Research Grant Council, University Grant Committee, Hong Kong SAR for the grant provided (Project nos. PolyU 152214/17E and PolyU 152064/18E). J Xuan would like to acknowledge the funding support from the Royal Society through Grant no. NAF\R1\180146. P. Tan would like to thank the CAS Pioneer Hundred Talents Program (KJ 2090130001), USTC Research Funds of the Double First-Class Initiative (YD 2090002006), and USTC Tang Scholar for providing the funding support. Y. Zhang gratefully acknowledges the financial support from the Natural Science Foundation of China (21673062).

Contributions

H.X. proposed the idea, conducted the multi-physics simulation, performed data management and drafted the manuscript. J.M. developed the deep neural network and genetic algorithm. P.T., Z.W. and Y.Z. interpreted the results. All authors edited and reviewed the manuscript. J.X. and M.N. supervised the work.

Nomenclature

Abbreviations

DL	Deep learning
DNN	Deep neural network
GA	Genetic algorithm
LSM	Lanthanum strontium manganite
MPS	Multi-physics simulation
sccm	Standard cubic centime per minute
ScSZ	Scandium stabilized zirconium
SOEC	Solid oxide electrolysis cell
TPB	Triple phase boundary
WGSR	Water gas shift reaction

Roman

$\mathrm{B_0}$	Permeability coefficient, m^2
$\mathrm{c_{CO_2}}$	Mole concentration of carbon dioxide, $mol \cdot m^{-3}$
$\mathrm{c_{H_2O}}$	Mole concentration of water, $mol \cdot m^{-3}$
$\mathrm{C_p}$	Heat capacity at constant pressure
$\mathrm{D_i^{eff}}$	Effective diffusivity of species i, $m^2 \cdot s^{-1}$
$\mathrm{D_{ik}^{eff}}$	Knudsen diffusion coefficient of i, $m^2 \cdot s^{-1}$
$\mathrm{D_{im}^{eff}}$	Molecular diffusion coefficient of i, $m^2 \cdot s^{-1}$
$\mathrm{E_{act}}$	Activation energy, $J \cdot mol^{-1}$
$\mathrm{E_{eq,CO_2}}$	Equilibrium potential for electrochemical CO_2 reduction, V
$\mathrm{E_{eq,CO_2}^0}$	Standard equilibrium potential for electrochemical CO_2 reduction, V
$\mathrm{E_{eq}}$	Equilibrium Nernst potential, V
$\mathrm{E_{eq,H_2O}}$	Equilibrium potential for electrochemical H_2O reduction, V
$\mathrm{E_{eq,H_2O}^0}$	Standard equilibrium potential for electrochemical H_2O reduction, V

F	Faraday constant, 96485 C·mol^{-1}
i	Operating current density, A·m^{-2}
i_o	Exchange current density, A·m^{-2}
n	Number of electrons transferred per electrochemical reaction
N_i	Flux of mass transport, kg·m^{-3}·s^{-1}
p	(partial) Pressure, Pa
P_{CO}^{L}	Local CO partial pressures, Pa
$P_{CO_2}^{L}$	Local CO_2 partial pressures, Pa
$P_{H_2}^{L}$	Local H_2 partial pressures, Pa
$P_{H_2O}^{L}$	Local H_2O partial pressures, Pa
$P_{O_2}^{L}$	Local O_2 partial pressures, Pa
R	Gas constant, 8.314 J·mol^{-1}·K^{-1}
R_{SMR}	Steam methane reforming reaction
R_{WGSR}	Water gas shift reaction
T	Temperature, K
TNC	Thermal neutral condition
TNP	Thermal neutral point
u	Velocity field, m^{3}·s^{-1}
V	Volume fraction
x_i	
y_i	Mole fraction of component i

Greek letters

α	Charge transfer coefficient
ε	Porosity

η_{act}	Activation overpotential loss, V
η_{ohmic}	Ohmic overpotential loss, V
κ	Permeability, m^2
λ	Heat conductivity
μ	Dynamic viscosity of fluid, Pa·s
ρ	Fluid density, kg·m^{-3}
σ	Conductivity, S·m^{-1}
γ	Pre-exponential factor, A m^{-2}
τ	Tortuosity

Subscripts

an	Anode
ca	Cathode
CO	Carbon monoxide
CO_2	Carbon dioxide
el	Electrolyte
H_2	Hydrogen
l	Ionic phase
O_2	Oxygen
s	Electronic phase

Superscripts

0	Parameter at equilibrium conditions
eff	Effective
L	Local

Reference

1. Giddings, B., Hopwood, B. & O’Brien, G. Environment, economy and society: fitting them together into sustainable development. *Sustain. Dev.* **10**, 187–196 (2002).

2. Cavicchioli, R. *et al.* Scientists’ warning to humanity: microorganisms and climate change. *Nat. Rev. Microbiol.* **17**, 569–586 (2019).

3. Saeidi, S., Amin, N. A. S. & Rahimpour, M. R. Hydrogenation of CO2 to value-added products—A review and potential future developments. *J. CO2 Util.* **5**, 66–81 (2014).

4. Hauch, A. *et al.* Recent advances in solid oxide cell technology for electrolysis. *Science (80-.).* **370**, eaba6118 (2020).

5. Laguna-Bercero, M. A. Recent advances in high temperature electrolysis using solid oxide fuel cells: A review. *J. Power Sources* **203**, 4–16 (2012).

6. Duan, C. *et al.* Highly efficient reversible protonic ceramic electrochemical cells for power generation and fuel production. *Nat. Energy* **4**, 230–240 (2019).

7. Götz, M. *et al.* Renewable Power-to-Gas: A technological and economic review. *Renew. Energy* **85**, 1371–1390 (2016).

8. Xu, H., Maroto-Valer, M. M., Ni, M., Cao, J. & Xuan, J. Low carbon fuel production from combined solid oxide CO2 co-electrolysis and Fischer-Tropsch synthesis system: A modelling study. *Appl. Energy* **242**, 911–918 (2019).

9. Kazempoor, P. & Braun, R. J. Hydrogen and synthetic fuel production using high temperature solid oxide electrolysis cells (SOECs). *Int. J. Hydrogen Energy* **40**, 3599–3612 (2015).

10. Hosseini, S. E. Design and analysis of renewable hydrogen production from biogas by integrating a gas turbine system and a solid oxide steam electrolyzer. *Energy Convers. Manag.* **211**, 112760 (2020).

11. Xu, H. *et al.* Performance improvement of a direct carbon solid oxide fuel cell through integrating an Otto heat engine. *Energy Convers. Manag.* **165**, 761–770 (2018).

12. Song, Y., Zhang, X., Xie, K., Wang, G. & Bao, X. High-Temperature CO2 Electrolysis in Solid Oxide Electrolysis Cells: Developments, Challenges, and Prospects. *Adv. Mater.* **31**, 1902033 (2019).

13. Xu, H. *et al.* The thermal effects of all porous solid oxide fuel cells. *J. Power Sources* **440**, 227102 (2019).

14. Mansilla, C., Sigurvinsson, J., Bontemps, A., Maréchal, A. & Werkoff, F. Heat management for hydrogen production by high temperature steam electrolysis. *Energy* **32**, 423–430 (2007).

15. Stempien, J. P., Ni, M., Sun, Q. & Chan, S. H. Thermodynamic analysis of combined Solid Oxide Electrolyzer and Fischer–Tropsch processes. *Energy* **81**, 682–690 (2015).

16. Chen, B., Xu, H. & Ni, M. Modelling of SOEC-FT reactor: Pressure effects on methanation process. *Appl. Energy* **185**, 814–824 (2017).

17. Pashchenko, D. Pressure drop in the thermochemical recuperators filled with the catalysts of various shapes: A combined experimental and numerical investigation. *Energy* **166**, 462–470 (2019).

18. Andersson, M., Yuan, J. & Sundén, B. SOFC modeling considering electrochemical reactions at the active three phase boundaries. *Int. J. Heat Mass Transf.* **55**, 773–788 (2012).

19. Luo, Y., Shi, Y., Li, W. & Cai, N. Synchronous enhancement of H2O/CO2co-electrolysis and methanation for efficient one-step power-to-methane. *Energy Convers. Manag.* **165**, 127–136 (2018).

20. Xu, H. *et al.* Towards online optimisation of solid oxide fuel cell performance: Combining deep learning with multi-physics simulation. *Energy AI* **1**, 100003 (2020).

21. Attia, P. M. *et al.* Closed-loop optimization of fast-charging protocols for batteries with machine learning. *Nature* **578**, 397–402 (2020).

22. Eriksson, E. L. V & Gray, E. M. Optimization and integration of hybrid renewable energy hydrogen fuel cell energy systems – A critical review. *Appl. Energy* **202**, 348–364 (2017).

23. Gu, G. H., Noh, J., Kim, I. & Jung, Y. Machine learning for renewable energy materials. *J. Mater. Chem. A* **7**, 17096–17117 (2019).

24. Schmidt, J., Marques, M. R. G., Botti, S. & Marques, M. A. L. Recent advances and applications of machine learning in solid-state materials science. *npj Comput. Mater.* **5**, 83 (2019).

25. Tabor, D. P. *et al.* Accelerating the discovery of materials for clean energy in the era of smart automation. *Nat. Rev. Mater.* **3**, 5–20 (2018).

26. Li, W., Wang, H., Shi, Y. & Cai, N. Performance and methane production characteristics of H2O–CO2 co-electrolysis in solid oxide electrolysis cells. *Int. J. Hydrogen Energy* **38**, 11104–11109 (2013).

27. Xu, H., Chen, B., Irvine, J. & Ni, M. Modeling of CH 4 -assisted SOEC for H 2 O/CO 2 co-electrolysis. *Int. J. Hydrogen Energy* **41**, 21839–21849 (2016).

28. Xu, H. *et al.* Modeling of all porous solid oxide fuel cells. *Appl. Energy* **219**, 105–113 (2018).

29. Todd, B. & Young, J. B. Thermodynamic and transport properties of gases for use in solid oxide fuel cell modelling. *J. Power Sources* **110**, 186–200 (2002).

30. Arriagada, J., Olausson, P. & Selimovic, A. Artificial neural network simulator for SOFC performance prediction. *J. Power Sources* **112**, 54–60 (2002).

31. Yan, Z., He, A., Hara, S. & Shikazono, N. Modeling of solid oxide fuel cell (SOFC) electrodes from fabrication to operation: Microstructure optimization via artificial neural networks and multi-objective genetic algorithms. *Energy Convers. Manag.* **198**, 111916 (2019).

32. Jiang, H., Xi, Z., A. Rahman, A. & Zhang, X. Prediction of output power with artificial neural network using extended datasets for Stirling engines. *Appl. Energy* **271**, 115123 (2020).

33. Chollet, F. & others. Keras. (2015).

34. Luo, Y., Shi, Y., Li, W. & Cai, N. Comprehensive modeling of tubular solid oxide electrolysis cell for co-electrolysis of steam and carbon dioxide. *Energy* **70**, 420–434 (2014).

35. Ni, M. An electrochemical model for syngas production by co-electrolysis of H2O and CO2. *J. Power Sources* **202**, 209–216 (2012).

List of Tables

Table 1. Governing Equations.

Table 2. Material properties.

Table 3. Kinetics of reactions.

Table 4. Operating parameters for model validation.

Table 5. Operating parameters for studying the effects of the gas flow rate and composition at the cathode inlet.

Table 6. Operating parameters for studying the effects of the gas temperature of the inlets.

Table 7. Operating parameters for the optimisation of TNCs.

Table 1. Governing Equations.

Electrochemical reaction model	
$H_2O + 2e^- = H_2 + O^{2-}$	Electrochemical reduction of H_2O
$CO_2 + 2e^- = CO + O^{2-}$	Electrochemical reduction of CO_2
$2O^{2-} = O_2 + 4e^-$	Electrochemical evolution of O_2
$H_2O = H_2 + 0.5O_2$	Overall electrochemical reaction of H_2O reduction
$CO_2 = CO + 0.5O_2$	Overall electrochemical reaction for CO_2 reduction
$E_{eq,H_2O} = E^0_{eq,H_2O} + \frac{RT}{2F}\ln\left[\frac{P^{L,C}_{H_2}(P^{L,A}_{O_2})^{1/2}}{P^{L,C}_{H_2O}}\right]$	Equilibrium potential for electrochemical reduction of H_2O
$E_{eq,CO_2} = E^0_{eq,CO_2} + \frac{RT}{2F}\ln\left[\frac{P^{L,C}_{CO}(P^{L,A}_{O_2})^{1/2}}{P^{L,C}_{CO_2}}\right]$	Equilibrium potential for electrochemical reduction of CO_2
$E^0_{eq,H_2O} = 1.253 - 0.00024516T\ (V)$	Standard potential for electrochemical reduction of H_2O
$E^0_{eq,CO_2} = 1.46713 - 0.0004527T\ (V)$	Standard potential for electrochemical reduction of CO_2
$V = E_{eq} - \eta_{act} - \eta_{ohmic}$	Calculation of applied voltage
$i = i_0\left\{\exp\left(\frac{\alpha nF\eta_{act}}{RT}\right) - \exp\left(-\frac{(1-\alpha)nF\eta_{act}}{RT}\right)\right\}$	Butler-Volmer equation
$i_l = -{\sigma_l}^{eff}\nabla(\emptyset_l)$	Calculation of ionic resistance
$i_s = -{\sigma_s}^{eff}\nabla(\emptyset_s)$	Calculation of electronic resistance
Chemical reaction model	
$CO + H_2O \leftrightarrow CO_2 + H_2$	Water gas shift reaction
Mass/Momentum transport	
$\frac{N_i}{D^{eff}_{ik}} + \sum_{j=1,j\neq i}^{n}\frac{y_jN_i - y_iN_j}{D^{eff}_{ij}} = -\frac{1}{RT}\left(\nabla(y_jP) + \frac{B_0y_jP}{\mu D^{eff}_{ik}}\nabla P\right)$	Extended Fick's model
$\nabla \cdot N_j = S_j$	Mass conservation equation
$\rho\frac{\partial u}{\partial t} + \rho u\nabla u = -\nabla p + \nabla[\mu(\nabla u + (\nabla u)^T) - \frac{2}{3}\mu\nabla u] - \frac{\varepsilon\mu u}{k}$	Navier-Stokes equation with Darcy's term
Heat transfer model	

$\rho C_p u \cdot \nabla T + \nabla \cdot (-\lambda_{eff} \nabla T) = Q$	General heat balance equation
$\lambda_{eff} = (1-\varepsilon)\lambda_s + \varepsilon\lambda_g$	Calculation of effective thermal conductivity

Table 2. Material properties [34].

Parameters	**Value / expression**	**Unit**
Conductivity		
σ_{ScSZ}	$69{,}200 \times e^{\frac{-9681}{T}}$	S m^{-1}
σ_{YSZ}	$33{,}400 \times e^{\frac{-10300}{T}}$	S m^{-1}
σ_{Ni}	$4.2 \times 10^6 - 1{,}065.3T$	S m^{-1}
σ_{LSM}	$4.2 \times 10^7 \exp(-1{,}150/T)$	S m^{-1}
Porosity		
ε_a	0.36	
ε_c	0.36	
Tortuosity		
τ_a	3	
τ_c	3	
Triple Phase Boundary		
S_{TPB}	2.14×10^5	m^{-1}
Heat Conductivity		

λ_a	9.6	W m^{-1} K^{-1}
λ_c	6.23	W m^{-1} K^{-1}
λ_{el}	2.7	W m^{-1} K^{-1}
Heat Capacity		
$C_{p,a}$	420	J kg^{-1} K^{-1}
$C_{p,c}$	390	J kg^{-1} K^{-1}
$C_{p,el}$	300	J kg^{-1} K^{-1}
Density		
ρ_a	6,570	kg m^{-3}
ρ_c	6,870	kg m^{-3}
ρ_{el}	2,000	kg m^{-3}

Table 3. Kinetics of reactions.

Parameters	**Value or expression**	**Unit**
Electrochemical Reaction		
i0	$\beta \cdot \exp\left(-\frac{E_a}{RT}\right)$	A m^{-2}
β	3.3×10^8	A m^{-2}
E_a	1.2×10^5	J mol^{-1}
α_{H_2O}	0.65	

α_{CO_2}	0.65	
Chemical Reaction		
R_{WGSR} [35]	$k_{sf}(p_{H_2O}p_{CO} - \frac{p_{H_2}p_{CO_2}}{K_{ps}})$	mol m^{-3} s^{-1}
k_{sf}	$0.0171\exp\left(\frac{-103191}{RT}\right)$	mol m^{-3} Pa^{-2} s^{-1}
K_{ps}	$\exp(-0.2935Z^3 + 0.6351Z^2 + 4.1788Z + 0.3169)$	
Z	$\frac{1000}{T} - 1$	

Table 4. Operating parameters for model validation.

Parameter	**Value**	**Unit**
Cathode gas flow rate	350	sccm
Anode gas flow rate	350	sccm
Cathode gas composition	28.6% CO_2 + 28.6% H_2O + 14.3% H_2 + 28.6% Ar	
Anode gas composition	Air (O_2, 21% + N_2, 79%)	
Gas temperature at inlets	1123	K
Applied voltage	0.9 – 1.4	V

Table 5. Operating parameters for studying the effects of the gas flow rate and composition at the cathode inlet.

Parameter	Value	Unit
Cathode gas flow rate	300 - 600	sccm
Anode gas flow rate	400	sccm
Cathode gas composition	H_2O (10% - 90%) + CO_2 (rest)	
Anode gas composition	Air (O_2, 21% + N_2, 79%)	
Gas temperature at inlets	1073	K
Applied voltage	0.9 – 1.6	V

Table 6. Operating parameters for studying the effects of the gas temperature of the inlets.

Parameter	Value	Unit
Cathode gas flow rate	400	sccm
Anode gas flow rate	400	sccm
Cathode gas composition	H_2O (50%) + CO_2 (50%)	
Anode gas composition	Air (O_2, 21% + N_2, 79%)	
Gas temperature at inlets	1023, 1123	K
Applied voltage	0.9 – 1.6	V

Table 7. Operating parameters for the optimisation of TNCs.

Parameter	Value	Unit
Anode gas flow rate	300 - 600	sccm
Cathode gas flow rate	400	sccm
Anode gas composition	H_2O (10% - 90%) + CO_2 (rest)	
Cathode gas composition	Air (O_2, 21% + N_2, 79%)	

Gas temperature at inlets	1023 - 1123	K
Applied voltage	0.9 – 1.6	V

List of Figures

Fig. 1 The schematic of an SOEC for H2O and CO2 co-electrolysis.

Fig. 2 The workflow of the hybrid method for the optimisation of SOECs.

Fig. 3 Comparison of V-I characteristics between the simulation results and the experimental data.

Fig. 4 The change of correlation coefficient and least mean square error in training and testing sets with the growth of epochs.

Fig. 5 The distribution of relative errors in predicting the current density, fuel generation rate and heat generation using DNN.

Fig. 6 Comparison of the SOEC performance at different applied voltages. The selected operating conditions are the combinations of flow rate (300/600 sccm) and gas composition (10%/90% H_2O) at the cathode inlet. (a) The voltage-current density relationship, (b) the voltage-H_2 generation rate relationship, (c) the voltage-heat generation relationship, and (d) the voltage-PTGrelationship.

Fig. 7 Comparison of the SOEC performance at different inlet gas temperatures of 1023 and 1123 K under different applied voltages. (a) The voltage-current density relationship, (b) the power density-voltage-H_2 generation rate relationship, (c) the voltage-heat generation relationship, and (d) the voltage-PTG relationship.

Fig. 8 (a) The distribution of required power density and applied voltage at different gas compositions and temperatures of cathode inlet under the TNC, (b) the voltage-temperature-gas composition relationship, (c) the voltage-power-gas composition relationship, and (d) the voltage-power-temperature relationship.

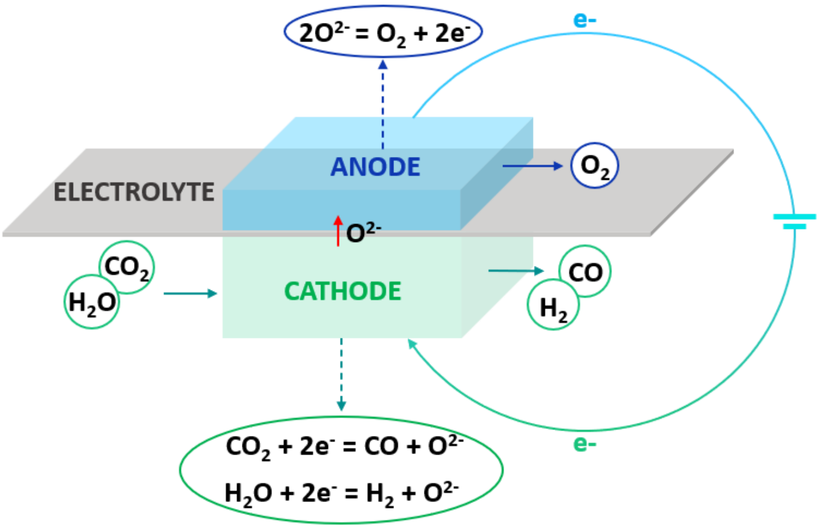

Fig. 1 The schematic of an SOEC for H2O and CO2 co-electrolysis.

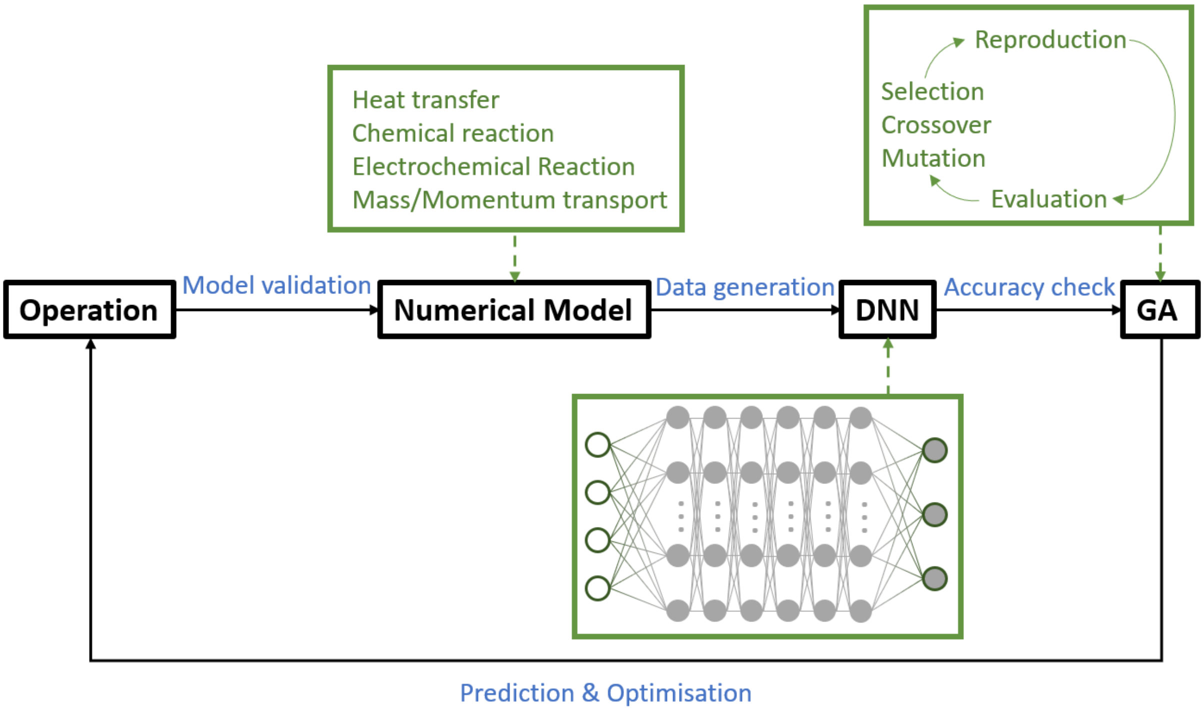

Fig. 2 The workflow of the hybrid method for the optimisation of SOECs.

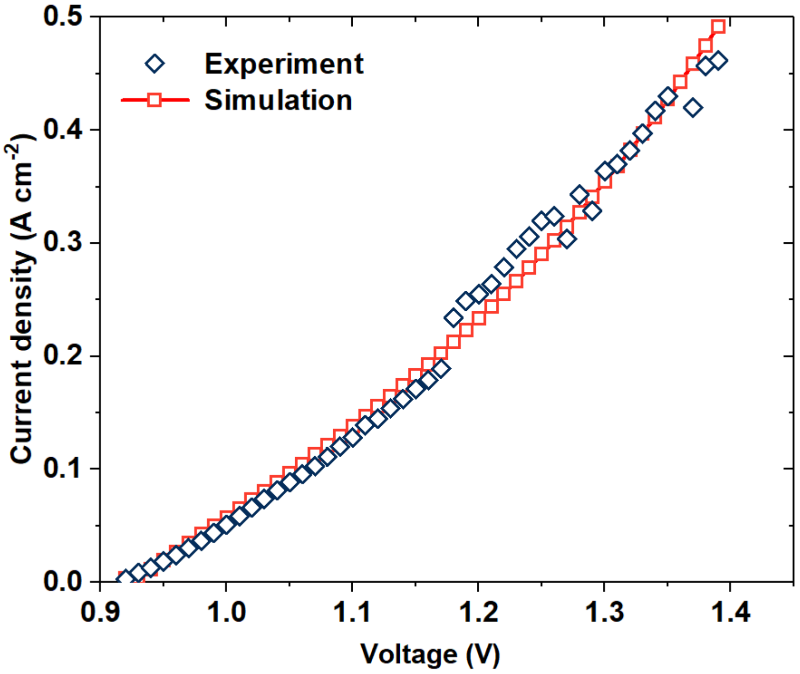

Fig. 3 Comparison of V-I characteristics between simulation results experimental data.

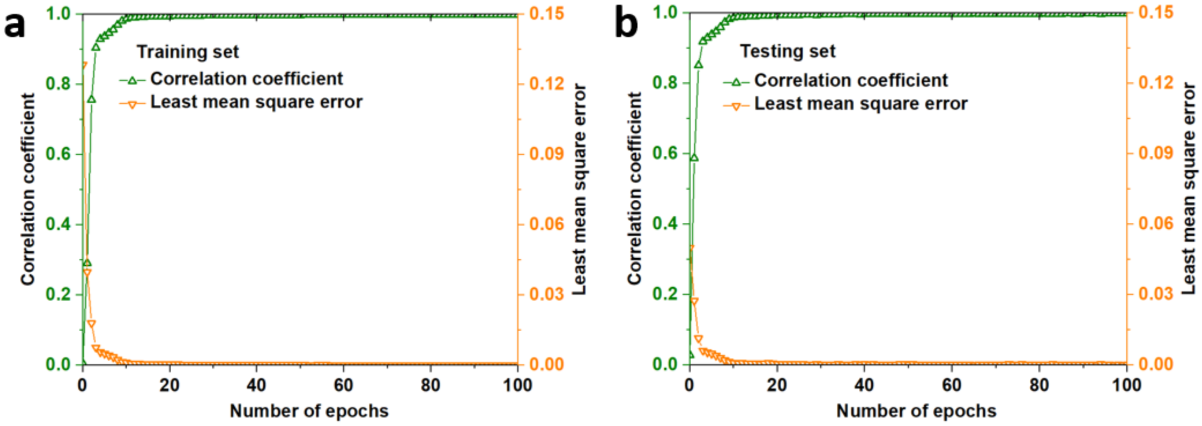

Fig. 4 The change of correlation coefficient and least mean square error in training and testing sets with the growth of epochs.

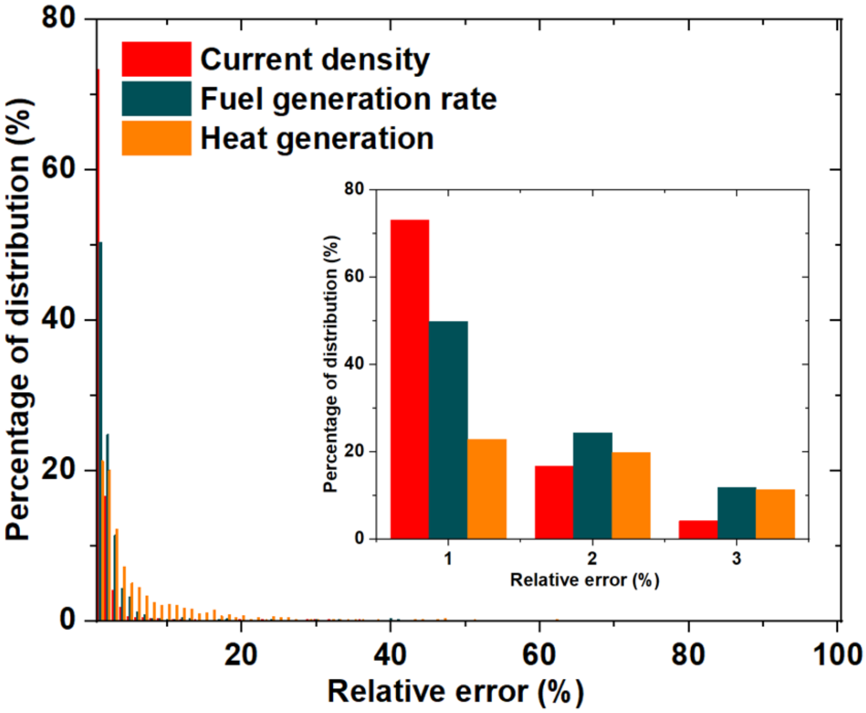

Fig. 5 The distribution of relative errors in predicting the current density, fuel generation rate and heat generation using DNN.

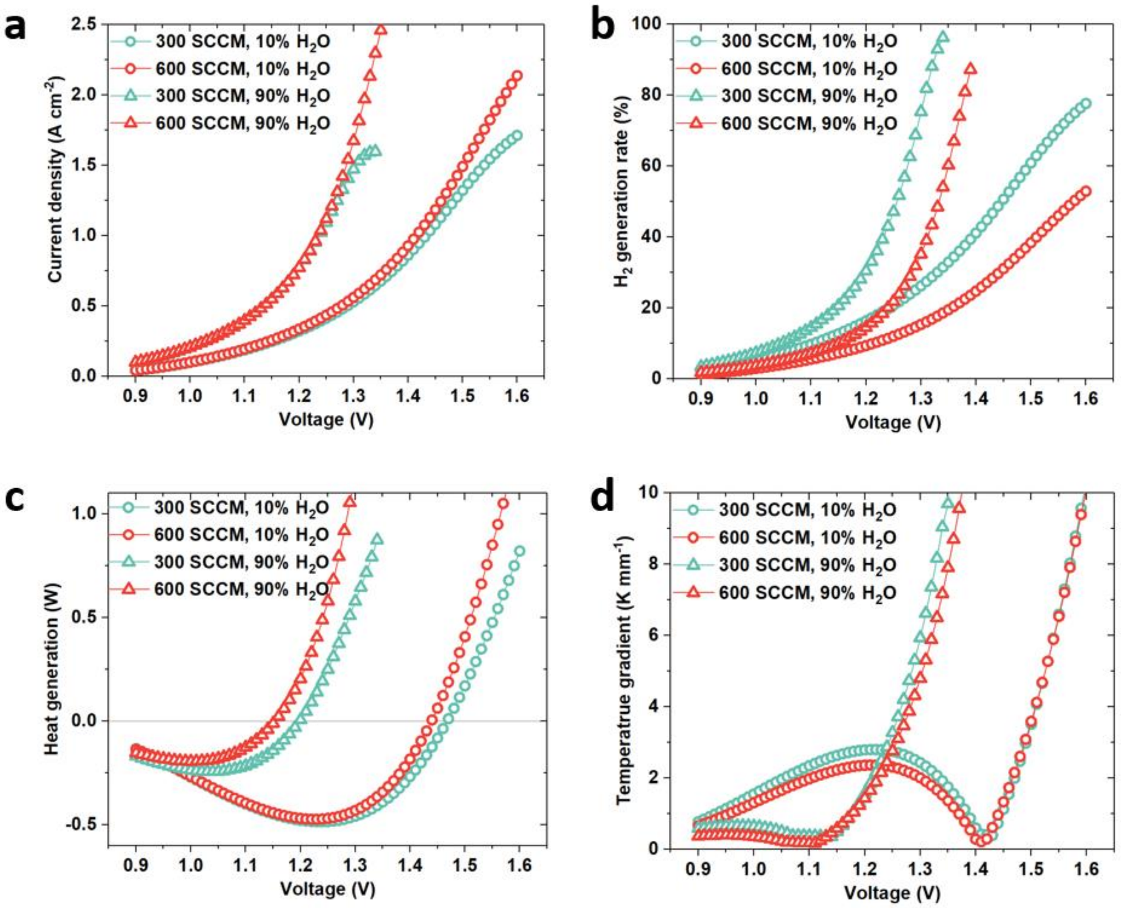

Fig. 6 Comparison of the SOEC performance at different applied voltages, the selected operating conditions are the combinations of flow rate (300/600 sccm) and gas composition (10%/90% H_2O) at the cathode inlet. (a) The voltage-current density relationship, (b) the voltage-H_2 generation rate relationship, (c) the voltage-heat generation relationship, and (d) the voltage-PTG relationship.

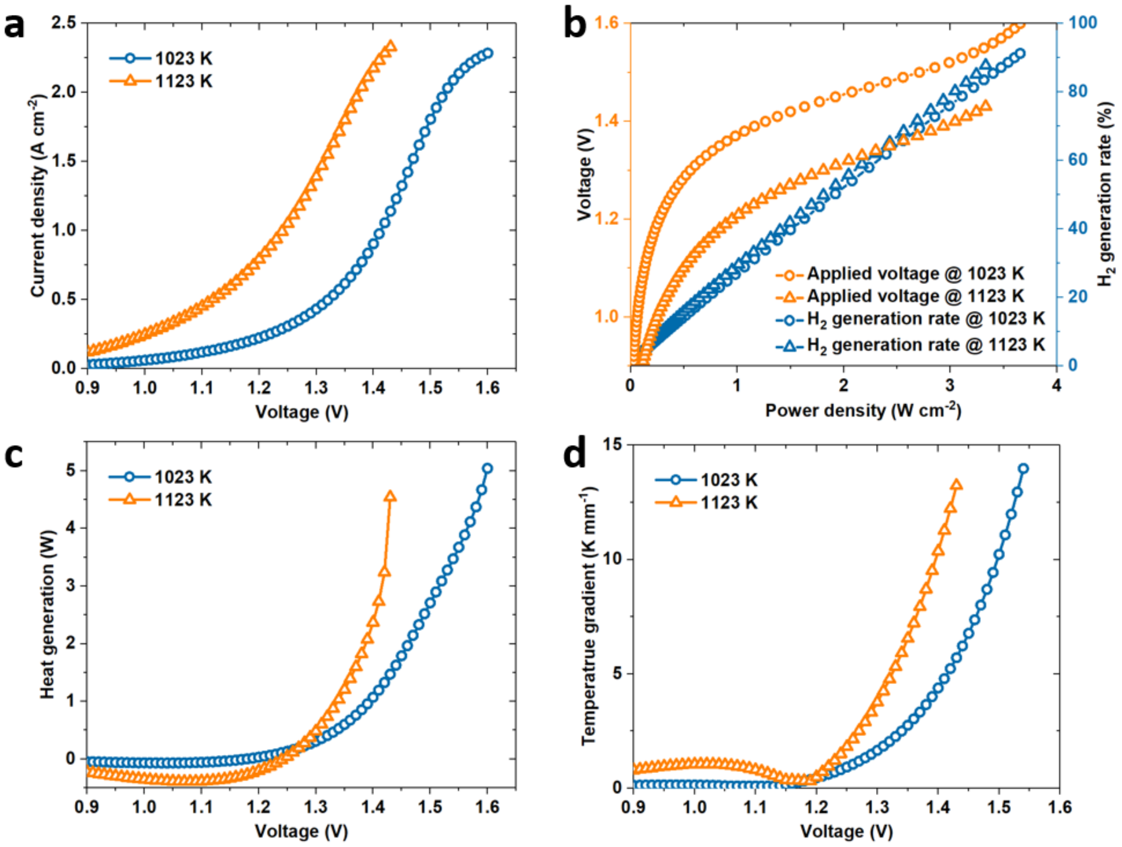

Fig. 7 Comparison of the SOEC performance at different inlet gas temperatures of 1023 and 1123 K under different applied voltages. (a) The voltage-current density relationship, (b) the power density-voltage-H_2 generation rate relationship, (c) the voltage-heat generation relationship, and (d) the voltage-PTG relationship.

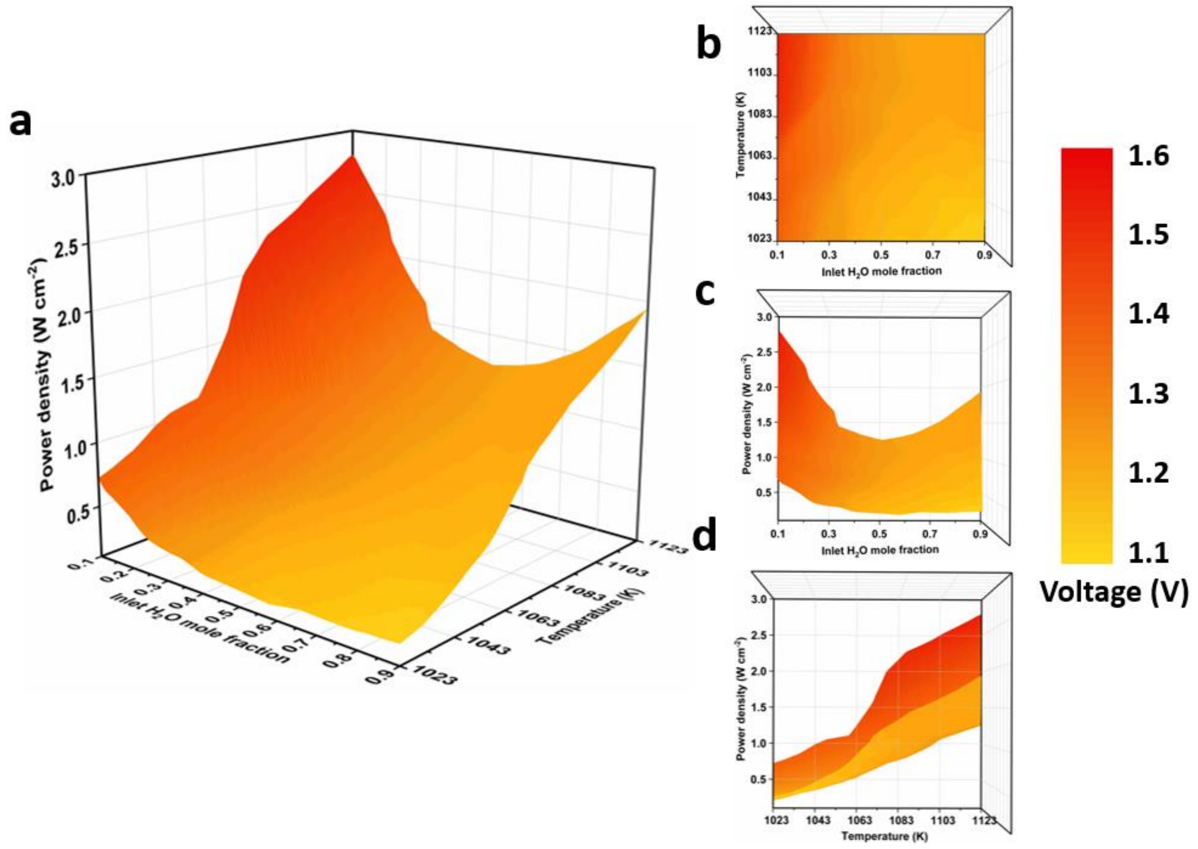

Fig. 8 (a) The distribution of required power density and applied voltage at different gas compositions and temperatures of cathode inlet under the TNC, (b) the voltage-temperature-gas composition relationship, (c) the voltage-power-gas composition relationship, and (d) the voltage-power-temperature relationship.